# Low-Complexity and Less-Conservativeness Ostrowski Stability Criterion for Parallel Fractional Grid-Connected Converters Under Unbalanced Grid

Bo Long, *Senior Member, IEEE*, Wandi Yang, JieFeng Hu, *Senior Member, IEEE*,
Jose Rodriguez, *Fellow, IEEE*, and Kil To Chong, *Member, IEEE*

***Abstract*—Three-level T-type converter (3LT$^2$C) with *LCL* filter have been widely used in renewable energy power generation system. Recent articles have shown that, due to the fractional characteristics of the inductance and capacitance of the *LCL* filter, the fractional-order model has higher accuracy than integer-order model in describing the static- and dynamic-behaviors of the physical *LCL*-3LT$^2$C converter. To evaluate the stability of the grid-connected fractional *LCL*-3LT$^2$C, fractional impedance model is often used. However, due to the fractional calculus, the overall order of the characteristic equation would increase, thus leading to high computation burden. Existing eigenvalues estimation method is not accurate enough for excessive estimation range. To solve these problems, a low-complexity and less-conservative stability criteria based on Ostrowski theorem is proposed, which determines the critical stability point according to the system loop gain matrix. First, the fractional sequence admittance models for a single and multiparallel F3LT$^2$C are established under unbalanced grid. Second, the critical stability points of the system are determined by Ostrowski theorem. Simulation and experimental results verify the modeling accuracy of the proposed fractional model and the effectiveness of the proposed stability theorem in low-complexity and less-conservativeness.**

***Index Terms*—Fractional inductor and capacitor, Gershgorin theorem, Ostrowski theorem, stability margin, T-type grid-connected converter.**

## I. INTRODUCTION

WITH the increasing integration of renewable energy into power grid [1], compared with the single converter, the multiparallel grid-connected converter (MP-GCC) [2] plays a more important role in increasing power capacity, enhancing the reliability and reducing the current harmonics [3]. However, the presence of unbalanced grid conditions [4], i.e., the multiphase short-circuit fault and unbalanced load [5], which poses significant challenges to the stability and output current quality of MP-GCC. Therefore, it is crucial to determine the critical stable resonance point of MP-GCC under unbalanced grid.

The power and control parts of traditional system modeling are often modeled by integer-order calculus. However, more and more studies have shown that active devices such as actual inductors [6] and capacitors [7] often exhibit fractional order (FO) calculus characteristics in actual circuits. Therefore, using fractional calculus theorem, the more accurate FO system mathematical model can be established. It will be closer to the actual physical model and the error is smaller, which is conducive to the subsequent research and analysis based on the system mathematical model.

At present, the modeling of FO systems mainly focuses on the circuit model containing fractional inductance and capacitance, and the fractional controller model, such as FO commande robuste d'Ordre non entier (CRONE) control, FO proportional-integral-deriative (PID) controller, fractional-order sliding-model control [8], etc. The modeling of FO power electronic converters is mainly divided into two categories, FO modeling in time-domain and frequency-domain.

In terms of time-domain modeling, most studies choose the state-space model to analyze the FO system. In [9], a sliding FO control safety was applied with the state-space model of multilevel converter, which improved the system robustness under system parameter uncertainties and nonlinear load alterations. In [10], a robust adaptive fuzzy FO nonsingular terminal sliding-mode controller was used to improve the output voltage tracking ability of dc/dc buck converters. In [11], to eliminate the disturbance, a high-order nonlinear disturbance observer based

Manuscript received 19 December 2023; revised 9 March 2024 and 21 April 2024; accepted 19 May 2024. Date of publication 22 May 2024; date of current version 16 July 2024. This work was supported in part by the Natural Science Foundation of Sichuan Province under Grant 23NSFSC0294, in part by Guangdong Basic and Applied Basic Research Foundation under Grant 2023A1515240058, in part by the Funding for Chengdu Science and Technology Bureau level International Cooperation Projects under Grant 2023-GH02-00014-HZ). Recommended for publication by Associate Editor M. Molinas. *(Corresponding author: Bo Long.)*

Bo Long and Wandi Yang are with the School of Mechanical and Electrical Engineering, University of Electronic Science and Technology of China (UESTC), 611731, China, also with the Yangtze Delta Region Institute (Huzhou), UESTC, Huzhou 313001, China, and also with the Institute of Electronic and Information Engineering of UESTC in Guangdong, 523808, China (e-mail: longbouestc1980@126.com; 202121040318@std.uestc.edu.cn).

JieFeng Hu is with the Centre for New Energy Transition Research, Federation University Australia, Mount Helen, VIC 3353, Australia, also with the Future Regions Research Centre, Federation University Australia, Mount Helen, VIC 3353, Australia (e-mail: j.hu@federation.edu.au).

Jose Rodriguez is with the Faculty of Engineering, Universidad Andres Bello, Santiago 8370146, Chile (e-mail: jose.rodriguez@unab.cl).

Kil To Chong is with the Department of Electronics and Information Engineering, Jeonbuk National University, Jeonju 54896, South Korea (e-mail: kitchong@jbnu.ac.kr).

Color versions of one or more figures in this article are available at https://doi.org/10.1109/TPEL.2024.3404356.

Digital Object Identifier 10.1109/TPEL.2024.3404356

on FO sliding-mode control strategy was proposed for Buck converters, which also used the state space model.

On other hands, the FO modeling in frequency-domain mainly focuses on the impedance modeling. In [12], a fractional active damping control with a more tuning parameter for grid-connected converter high-power photovoltaic systems was proposed, which robustly mitigated the passive filter resonance and improve the power quality. In [13], the coupling between the doubly-fed induction generator and the grid was analyzed, which proposed fractional damping to enhance the system robustness and improve the tracking ability of the phase-lock-loop (PLL).

The stability analysis for different system models can be divided into two types, time- and frequency-domain [14], [15]. The stability of the system in time-domain is determined by the eigenvalues of the state-space equation. For example, the reduced-order Jacobian matrix criterion was applied to analyze the stability characteristics of grid-connected converters [16]. In [17] and [18], Lyapunov stability theorem and Floquet theorem were proposed with the small-signal state-space model to determine the system stability of multilevel converters. These stability analysis methods can help estimating the parameter range of the controller. However, the time-domain stability analysis is based on the state-space model. When the grid voltage falls within unbalanced conditions, it becomes difficult to separate the negative- and positive-sequence.

In frequency-domain, there are many classical methods to analyze, i.e., the Routh criterion, impedance ratio criterion and Nyquist stability criterion [19]. In [20], the Nyquist stability criterion was utilized to assess small-signal stability of grid-connected converter and the short time small-signal was injected to the reference current of control loop to identify the grid impedance. In [21], a discrete generalized Bode criterion was proposed, which combined the Nyquist criterion and open loop Bode diagram to analyze the stability of the impedance of the three-phase converter. Compared with the impedance model, admittance model is more suitable for the FLCL-3LT$^2$C in parallel connection [22].

Traditional Nyquist stability criterion needs to calculate the eigenvalues, however, for high-order complex converter-grid coupling system, the calculation of the eigenvalues is often very complicated for fractional system. To reduce the calculation burden, an eigenvalue estimation method based on the system model was often used for stability analysis. In [23], the calculation of eigenvalues in conventional Nyquist criterion was simplified by estimating the eigenvalue range by Gershgorin discs theorem.

Gershgorin theorem is one of the discs theories, which is also the basis of using inverse Nyquist array of multivariable frequency control. It has been already used in [24] to estimate the controller and PLL parameter range of a double-fed induction generator when the system is in stable operation. While another disc theorem, Ostrowski theorem, has narrower circular bands in the complex plane than those computed by Gershgorin theorem, and therefore has a more accurate and less conservative range of eigenvalues estimation. Accordingly, this article applied the Ostrowski stability criterion to estimate the range of the eigenvalue of the loop gain matrix to determine the critical stability point, and compared the results with those calculated by Gershgorin theorem.

In summary, the main contribution of this article is summarized as follows.

1) Based on the fractional calculus, fractional model of the *LCL*-3LT$^2$C established, which is proved to have higher accuracy by comparing it with the integer-order mathematical model and the physical object.
2) The Ostrowski theorem is combined with the fractional admittance model to calculate the stability margin and justify the critical stability point of the parallel connection converter under unbalanced grid. This improved stability criterion could reduce the computational complexity and the operation time.
3) Experimental results of the critical stability points calculated by different methods verify the low conservativeness and higher accuracy of the proposed method.

The rest of this article is organized as follows. Section II introduces the power circuit of FLCL-3LT$^2$C based on fractional calculous. Sections III and IV give the sequence fractional admittance model for a single and parallel FLCL-3LT$^2$C under unbalanced grid. Based on the loop gain matrix, Section V compares the stability critical point calculated by Gershgorin and Ostrowski theorems. Section IV illustrates the experimental results, which validates the effectiveness of the proposed method under two scenarios. Finally, Section VII concludes this article.

## II. POWER CIRCUIT OF FRACTIONAL GRID-CONNECTED LCL-3LT$^2$C CONVERTER

### *A. Preliminary of Fractional Order Calculus*

The concept of FO calculus is extended from the integers to the real axis and even the whole complex plane. Depending on the needs, the main definitions of FO operators are currently Grunwald–Letnikov (GL), Riemann–Liouville, and Caputo(C) definitions, but all three calculus definitions have the same general expression as

$$D_t^{\alpha} f(t) = \begin{cases} \frac{d^{\alpha} f(t)}{dt^{\alpha}}, \alpha > 0 \\ f(t), \alpha = 0 \\ \int_{t_0}^{t} f(\tau) d\tau^{\alpha}, \alpha < 0 \end{cases} \tag{1}$$

where $D_t^{\alpha}$ is the FO calculus operator, $\alpha$ is the FO. According to the existing research, the order of FO inductor and capacitor is positive. Based on (1), the comparison of electrical characteristics of FO and integer order (IO) of inductor and capacitor in time- domain and frequency-domain can be obtained, as given in Table I.

### *B. Topology Description*

The topology of parallel-connected fractional-order three phase T-type converter with *LCL* filter is demonstrated in Fig. 1, which contains two parts: power module and control module.

In Fig. 1, two series connected capacitors $C_1$ and $C_2$ are set at the dc-link, then twelve power transistors are denoted as $T_{a1}$ to $T_{a4}$, $T_{b1}$ to $T_{b4}$ and $T_{c1}$ to $T_{c4}$. The fractional LCL filter is composed of fractional inductance $L_1$ and $L_2$, fractional

TABLE I
COMPARISON BETWEEN FO- AND IO-INDUCTANCE AND CAPACITANCE

| | Inductance | | Capacitance | |
|---|---|---|---|---|
| | **FO** | **IO** | **FO** | **IO** |
| $x(t)$ | $u_L = L\frac{d^\alpha i_L}{dt^\alpha}$ | $u_L = L\frac{di_L}{dt}$ | $u_C = \frac{1}{C}\int_0^t i_C(t)dt^\beta$ | $u_C = \frac{1}{C}\int_0^t i_C(t)dt$ |
| Order | $0 < \alpha < 2$ | $\alpha = 1$ | $0 < \beta < 2$ | $\beta = 1$ |
| $Z(s)$ | $Ls^\alpha$ | $Ls$ | $1/(Cs^\beta)$ | $1/(Cs)$ |

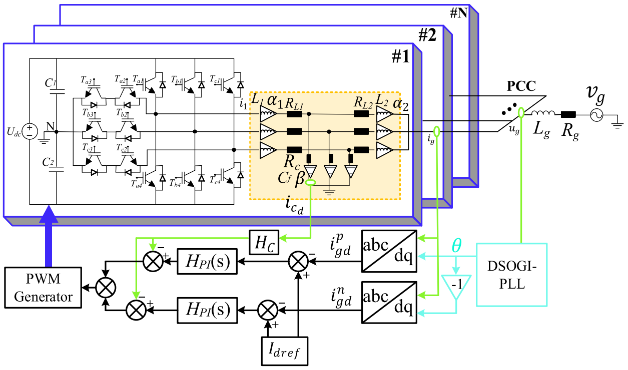

Fig. 1. Power circuit topology of a FLCL-3LT$^2$C.

capacitance $C_f$ and their parasitic resistances $R_{L1}$, $R_{L2}$, $R_C$. $\boldsymbol{e}$, $\boldsymbol{i}_1$, $\boldsymbol{v_C}$, $\boldsymbol{i_C}$ are converter voltage and current, capacitance voltage and current respectively. At the grid side, the converters are parallel connected at the point of common coupling (PCC) while the grid impedance is formed of $L_g$ and $R_g$. $v_g$ and $i_g$ are the grid voltage and current.

The controller contains the duel second order general integrator PLL, the $abc - dq$ frame transformation module, the current regulator and pulsewidth modulator generator. The capacitor current feedback module is the constant $H_C$. $\alpha_1$, $\alpha_2$ and $\beta$ are the FO of $L_1$, $L_2$ and $C_f$, respectively.

## III. SEQUENCE ADMITTANCE MODEL UNDER UNBALANCED GRID

### A. Sequence Separation of the Grid Voltage and Current

According to the method of symmetrical components and due to the absence of zero sequence in the grid connected converter, the unbalanced grid voltage of FLCL-3LT$^2$C could be decomposed into positive sequence and negative sequence. The grid voltage of phase $\boldsymbol{a}$ in time-domain $\boldsymbol{v_{ga}}$ can be decomposed as

$$\begin{aligned} \mathrm{v}_{ga} = {} & V_1\cos(\omega_0 t) + V_2\cos(\omega_0 t + \varphi_2) \\ & + V_p\cos(\omega_p t + \varphi_p) + V_n\cos(\omega_n t + \varphi_n) \end{aligned} \tag{2}$$

where $V_1$ and $V_2$represent the amplitude of positive- and negative-fundamental sequence, $\omega_0$ is fundamental angular frequency; $V_P$ and $V_n$ represent the amplitude of positive and negative perturbation sequence, $\omega_p$, $\omega_n$, $\varphi_p$ and $\varphi_n$ represent their angular frequency and their initial phase, respectively. Equation (2) could be transformed to frequency-domain by utilizing Fourier transform, which is given as

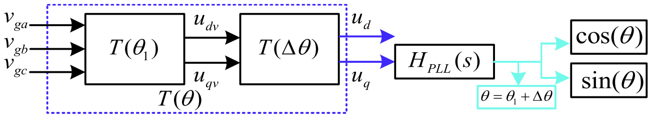

Fig. 2. $abc - dq$ transformation of PLL with $\Delta\theta$.

$$\mathrm{v}_{ga}[f] = \begin{cases} \boldsymbol{V}_1 + \boldsymbol{V_2} = (V_1/2)e + (V_2/2)e^{\pm j\varphi_2}, f = \pm f_1 \\ \boldsymbol{V_p} = (V_p/2)e^{\pm j\varphi_p}, f = \pm f_p \\ \boldsymbol{V_n} = (V_n/2)e^{\pm j\varphi_n}, f = \pm f_n \end{cases} \tag{3}$$

where $f_1$, $f_p$, $f_n$ are the fundamental, positive perturbation and negative perturbation frequency respectively. The frequency domain expression of the symmetrical components of grid current is similar to (3). It is derived in (4), where $I_1$ and $I_2$ represent the amplitude of positive and negative fundamental grid current sequence; $I_P$ and $I_n$ represent the amplitude of positive and negative perturbation sequence; $\varphi_{i1}$, $\varphi_{i2}$, $\varphi_{ip}$ and $\varphi_{in}$ are there initial phase angle, respectively,

$$\mathrm{i}_{ga}[f] = \begin{cases} \boldsymbol{I_1} + \boldsymbol{I}_2 = (I_1/2)e^{\pm j\varphi_{i1}} + (I_2/2)e^{\pm j\varphi_{i2}}, \\ \quad f = \pm f_1 \\ \boldsymbol{I_p} = (I_p/2)e^{\pm j\varphi_{ip}}, f = \pm f_p \\ \boldsymbol{I_n} = (I_n/2)e^{\pm j\varphi_{in}}, f = \pm f_n \end{cases}. \tag{4}$$

### B. Small-Signal Model of PLL

Since the controller requires the transformation of grid voltage and current from $abc$ to $dq$ frame, but due to the unbalanced grid including positive and negative sequence perturbation, the phase angle $\theta$ extracted by PLL is the sum of fundamental phase angle $\theta_1$ and error angle $\Delta\theta$ as Fig. 2.

Because $\Delta\theta$ is much smaller than $\theta$, assume $cos\Delta\theta \approx 1$, sin$\Delta\theta \approx \Delta\theta$, then $\boldsymbol{T}(\boldsymbol{\theta})$ is derived in (5), cos$\theta$ and sin$\theta$ are expressed as

$$\boldsymbol{T}(\boldsymbol{\theta}_1) = \begin{bmatrix} \cos\theta_1 & \cos\left(\theta_1 - \frac{2\pi}{3}\right) & \cos\left(\theta_1 + \frac{2\pi}{3}\right) \\ -\sin\theta_1 & -\sin(\theta_1 - \frac{2\pi}{3}) & -\sin\left(\theta_1 + \frac{2\pi}{3}\right) \\ \frac{1}{2} & \frac{1}{2} & \frac{1}{2} \end{bmatrix}$$

$$\boldsymbol{T}(\boldsymbol{\Delta\theta}) = \begin{bmatrix} \Delta\theta & 1 & 0 \\ -1 & \Delta\theta & 0 \\ 0 & 0 & 1 \end{bmatrix} \tag{5}$$

$$\begin{cases} \cos\theta \approx \cos\theta_1 - \sin\theta_1\Delta\theta \\ \sin\theta \approx \sin\theta_1 + \cos\theta_1\Delta\theta \end{cases}. \tag{6}$$

According to [25], under the influence of fundamental positive- and negative-sequence voltage $\boldsymbol{V}_1$ and $\boldsymbol{V}_2$, the perturbation components of positive- and negative-perturbation voltage $\boldsymbol{V_p}$ and $\boldsymbol{V_n}$ of $\Delta\theta$ in frequency-domain $\Delta\theta[f]$ are as follows:

$$\Delta\theta(f) = \begin{cases} \mp jG(s)\boldsymbol{V_p}, f = \pm(f_p - f_1) \\ \pm jG(s)\boldsymbol{V_n}, f = \pm(f_n + f_1) \\ \pm jF_p(s)\boldsymbol{V_p}\boldsymbol{V}_2, f = \pm(f_p + f_1) \\ \mp jF_n(s)\boldsymbol{V_n}\boldsymbol{V}_2^*, f = \pm(f_n - f_1) \end{cases},$$

$$\begin{cases} G(s) = H_{PLL}(s)/(1+V_1 H_{PLL}(s)) \\ F_p(s) = G(s)G(s \mp j4\pi f_1) \\ F_n(s) = G(s)G(s \pm j4\pi f_1) \end{cases} \tag{7}$$

where $H_{\mathrm{PLL}} = \frac{1}{s}(K_{p\mathrm{PLL}} + \frac{K_{i\mathrm{PLL}}}{s})$. Substituting (7) into (6) and apply Fourier Transform, then the frequency-domain expression for the sine- and cosine-components of $\theta$ are $\cos(\theta)[f]$ and $\sin(\theta)[f]$, are shown as

$$\cos(\theta)[f] = \begin{cases} 1/2, f = \pm f_1 \\ (G(s)\boldsymbol{V_p} + F_p(s)\boldsymbol{V_p}\boldsymbol{V}_2)/2, f = \pm f_p \\ -G(s)\boldsymbol{V_p}/2, f = \pm(f_p - 2f_1) \\ (G(s)\boldsymbol{V_n} + F_n(s)\boldsymbol{V_n}\boldsymbol{V}_2^*)/2, f = \pm f_n \\ -G(s)\boldsymbol{V_n}/2, f = \pm(f_n + 2f_1) \\ -F_p(s)\boldsymbol{V_p}\boldsymbol{V_2}/2, f = \pm(f_p + 2f_1) \\ -F_n(s)\boldsymbol{V_n}\boldsymbol{V}_2^*/2, f = \pm(f_n - 2f_1) \end{cases} \tag{8}$$

$$\sin(\theta)[f] = \begin{cases} \mp j/2, f = \pm f_1 \\ (\mp jG(s)\boldsymbol{V_p} \pm jF_p(s)\boldsymbol{V_p}\boldsymbol{V}_2)/2, f = \pm f_p \\ \pm jT_p\boldsymbol{V_p}/2, f = \pm(f_p - 2f_1) \\ (\mp jT_n\boldsymbol{V_n} \mp jF_n(s)\boldsymbol{V_n}\boldsymbol{V}_2^*)/2, f = \pm f_n \\ \pm jT_n\boldsymbol{V_n}/2, f = \pm(f_n + 2f_1) \\ \pm jF_p(s)\boldsymbol{V_p}\boldsymbol{V}_2/2, f = \pm(f_p + 2f_1) \\ \mp jF_n(s)\boldsymbol{V_n}\boldsymbol{V}_2^*/2, f = \pm(f_n - 2f_1) \end{cases}. \tag{9}$$

Substituting the output of PLL in frequency-domain in (5) with (8) and (9), the frequency-domain expression of the $abc-dq$ transformation matrix $\boldsymbol{T}(\boldsymbol{\theta})[f]$ could be obtained in (10), which contains the phase angle error $\Delta\theta$ caused by positive- and negative harmonic sequence voltage influenced by fundamental grid voltage

$$\boldsymbol{T}(\boldsymbol{\theta})[f] = \begin{bmatrix} \cos(\theta)[f] & \cos(\theta - \frac{2\pi}{3})[f] & \cos(\theta + \frac{2\pi}{3})[f] \\ -\sin(\theta)[f] & -\sin(\theta - \frac{2\pi}{3})[f] & -\sin(\theta + \frac{2\pi}{3})[f] \\ \frac{1}{2} & \frac{1}{2} & \frac{1}{2} \end{bmatrix}. \tag{10}$$

## C. *Current Regulator Model Under* dq*-Frame*

Applying the frame transformation matrix $\boldsymbol{T}(\boldsymbol{\theta})$ to (4), then the grid current in $dq$ frame with the positive- and negative-sequence coupling are shown as

$$\mathrm{i}_{gd}[f] = \begin{cases} I_1 \cos\varphi_{i1}, \quad f = 0 \\ \boldsymbol{I}_{2,} \ f = \pm 2f_1 \\ \boldsymbol{I_p} \mp j\sin\varphi_{i1} I_1 G(s)\boldsymbol{V_p}, \quad f = \pm(f_p - f_1) \\ \pm j\sin\varphi_{i1} I_1 F_p(s)\boldsymbol{V_p}\boldsymbol{V}_2, \quad f = \pm(f_p + f_1) \\ \boldsymbol{I_n} \pm j\sin\varphi_{i1} I_1 G(s)\boldsymbol{V_n}, \quad f = \pm(f_n - f_1) \\ \mp j\sin\varphi_{i1} I_1 F_n(s)\boldsymbol{V_p}\boldsymbol{V}_2^*, \quad f = \pm(f_n + f_1) \end{cases} \tag{11}$$

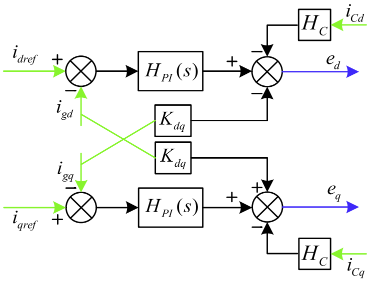

Fig. 3. Diagram of PI controller under *dq*-frame.

$$\mathrm{i}_{gq}[f] = \begin{cases} I_1 \sin\varphi_{i1}, \quad f = 0 \\ \pm j\boldsymbol{I}_{2,} \ f = \pm 2f_1 \\ \mp\boldsymbol{I_p} \pm j\cos\varphi_{i1} I_1 G(s)\boldsymbol{V_p}, \quad f = \pm(f_p - f_1) \\ \mp j\cos\varphi_{i1} I_1 F_p(s)\boldsymbol{V_p}\boldsymbol{V}_2, \quad f = \pm(f_p + f_1) \\ \pm j\boldsymbol{I_n} \pm jcoa\varphi_{i1} I_1 G(s)\boldsymbol{V_n}, \ f = \pm(f_n - f_1) \\ \pm j\cos\varphi_{i1} I_1 F_n(s)\boldsymbol{V_p}\boldsymbol{V}_2^*, \quad f = \pm(f_n + f_1) \end{cases}. \tag{12}$$

The current regulator has to transform the controlled variables from $abc$- to $dq$-frame, as shown in Fig. 3, where $i_{dref}$ and $i_{qref}$ are grid current reference; $i_{gd}$, $i_{gq}$ and $i_{Cd}$, $i_{Cq}$ are the sampling grid current and the filter capacitance current; $H_{PI}(s) = k_{pPI} + k_{iPI}/s$ is the proportional and integral controller; $K_{dq} = (L_1 + L_2)\omega_0$ is the decoupling constant; $H_C$ is the feedback constant of capacitance current.

Substituting the grid current in (11) and (12) with the variables in Fig. 3, the converter voltage in $dq$ frame $e_d$ and $e_q$ could be expressed with grid current and voltage given as

$$\begin{bmatrix} e_d \\ e_q \end{bmatrix} = H_{PI}(s)\begin{bmatrix} i_{dref} \\ i_{qref} \end{bmatrix} + \begin{bmatrix} M(s) & K_{dq} \\ -K_{dq} & M(s) \end{bmatrix}\begin{bmatrix} i_{gd} \\ i_{gq} \end{bmatrix} - C_f s^{\beta}\begin{bmatrix} v_{gd} \\ v_{gq} \end{bmatrix}$$
$$M(s) = C_f L_2 s^{(\alpha_2+\beta)} - H_{PI}(s). \tag{13}$$

The reference value of positive and negative perturbation grid current can be assumed to be suppressed to zero. Assuming the dc components of current regulator is $D_0$ and $Q_0$, they can be calculated through circuit equations at the operating point with fundamental frequency, as shown in [25]. Finally, the output of the current regulator in frequency-domain is given as

$$e_d[f] = \begin{cases} C_f L_2 s^{(\alpha_2+\beta)} I_1 \cos\varphi_{i1} - K_{dq} I_1 \sin\varphi_{i1} + D_0, f = 0 \\ M(s)\boldsymbol{I}_2 \pm jK_{dq}\boldsymbol{I}_2 - C_f s^{\beta}\boldsymbol{V}_2, f = \pm 2f_1 \\ \boldsymbol{I_p}(M(s) \pm K_{dq}) + jI_1 G(s)\boldsymbol{V_p}(\mp\sin\varphi_{i1}(M(s) \\ -C_f s^{\beta}) \mp \cos\varphi_{i1} K_{dq}), f = \pm(f_p - f_1) \\ jI_1 F_p(s)\boldsymbol{V_p}\boldsymbol{V}_2(\pm\sin\varphi_{i1}(M(s) - C_f s^{\beta}) \\ \mp\cos\varphi_{i1} K_{dq}), f = \pm(f_p + f_1) \\ \boldsymbol{I_n}(M(s) \pm jK_{dq}) + jI_1 G(s)\boldsymbol{V_n}(\pm\sin\varphi_{i1}(M(s) \\ -C_f s^{\beta}) \pm \cos\varphi_{i1} K_{dq}), f = \pm(f_n - f_1) \\ jI_1 F_n(s)\boldsymbol{V_n}\boldsymbol{V}_2^*(\mp\sin\varphi_{i1}(M(s) - C_f s^{\beta}) \\ \pm\cos\varphi_{i1} K_{dq}), f = \pm(f_n + f_1) \end{cases} \tag{14}$$

$$e_q[f] = \begin{cases} C_f L_2 s^{(\alpha_2+\beta)} I_1 \cos\varphi_{i1} - K_{dq} I_1 \sin\varphi_{i1} + Q_0, f = 0 \\ M(s)\boldsymbol{I}_2 \mp jK_{dq}\boldsymbol{I}_2 - C_f s^{\beta}\boldsymbol{V}_2, f = \pm 2f_1 \\ \boldsymbol{I_p}(M(s) \mp K_{dq}) + jI_1 G(s)\boldsymbol{V_p}(\pm\cos\varphi_{i1}(M(s) \\ \quad -C_f s^{\beta}) \pm \sin\varphi_{i1} K_{dq}), f = \pm(f_p - f_1) \\ jI_1 F_p(s)\boldsymbol{V_p}\boldsymbol{V}_2(\mp\cos\varphi_{i1}(M(s) \\ \quad -C_f s^{\beta}) \pm \sin\varphi_{i1} K_{dq}), f = \pm(f_p + f_1) \\ \boldsymbol{I_n}(M(s) \mp jK_{dq}) + jI_1 G(s)\boldsymbol{V_n}(\mp\cos\varphi_{i1}(M(s) \\ \quad -C_f s^{\beta}) \mp \sin\varphi_{i1} K_{dq}), f = \pm(f_n - f_1) \\ jI_1 F_n(s)\boldsymbol{V_n}\boldsymbol{V}_2^*(\pm\cos\varphi_{i1}(M(s) - C_f s^{\beta}) \\ \quad \mp \sin\varphi_{i1} K_{dq}), f = \pm(f_n + f_1) \end{cases} . \tag{15}$$

Applying inverse $abc - dq$ transformation matrix $\boldsymbol{T}^{-1}(\boldsymbol{\theta})$, the converter voltage $\boldsymbol{e}$ can be transformed to $abc$-frame expressed by positive- and negative-perturbation sequence of grid current and voltage, whose coefficient matrix $\boldsymbol{C_{ig}}$ and $\boldsymbol{C_{Vg}}$ can be derived from (14) and (15), and the converter-side voltage is given as follows:

$$\begin{bmatrix} e_a \\ e_b \\ e_c \end{bmatrix} = \boldsymbol{C_{ig}} \boldsymbol{A} \begin{bmatrix} \boldsymbol{I_p} \\ \boldsymbol{I_n} \\ 0 \end{bmatrix} + \boldsymbol{C_{vg}} \boldsymbol{A} \begin{bmatrix} \boldsymbol{V_p} \\ \boldsymbol{V_n} \\ 0 \end{bmatrix}, \boldsymbol{A} = \begin{bmatrix} 1 & 1 & 1 \\ \alpha^2 & \alpha & 1 \\ \alpha & \alpha^2 & 1 \end{bmatrix} \tag{16}$$

where $\alpha = e^{j2/3\pi}$.

### D. Sequence Admittance of a Single FLCL-3LT$^2$C Converter

*1) Admittance Model of a Single FLCL-3LT$^2$C:* Based on Kirchhoff's voltage law and the FO calculus, the circuit equation of a single FLCL-3LT$^2$C in frequency-domain under $abc$ frame is derived as

$$\begin{bmatrix} e_a \\ e_b \\ e_c \end{bmatrix} = (1 + L_1 C_f s^{(\alpha_1+\beta)}) \begin{bmatrix} v_{ga} \\ v_{gb} \\ v_{gc} \end{bmatrix} + \left(\mathrm{s}^{\alpha_1} L_1 + \mathrm{s}^{\alpha_2} L_2 + L_1 L_2 C_f s^{(\alpha_1+\alpha_2+\beta)}\right) \begin{bmatrix} i_{ga} \\ i_{gb} \\ i_{gc} \end{bmatrix}. \tag{17}$$

Substituting the converter voltage in (17) with (16) and convert the grid voltage and current to positive and negative sequence expressions, then the output admittance of FLCL-3LT$^2$C is derived

$$\begin{bmatrix} \boldsymbol{I_p} \\ \boldsymbol{I_n} \end{bmatrix} = -\boldsymbol{Y_o} \begin{bmatrix} \boldsymbol{V_p} \\ \boldsymbol{V_n} \end{bmatrix} = -\begin{bmatrix} Y_{PP} & Y_{pn} \\ Y_{nP} & Y_{nn} \end{bmatrix} \begin{bmatrix} \mathbf{V}_{\boldsymbol{p}} \\ \boldsymbol{V_n} \end{bmatrix} \tag{18}$$

where the expression of $\boldsymbol{Y_o}$ is as (19) and $\boldsymbol{I}$ is $2 \times 2$ identity matrix

$$\boldsymbol{Y}_{\mathbf{o}} = \frac{\boldsymbol{C_{vg}} - (1 + L_1 C_f s^{(\alpha_1+\beta)})\boldsymbol{I}}{\boldsymbol{C_{ig}} - \left(\mathrm{s}^{\alpha_1} L_1 + \mathrm{s}^{\alpha_2} L_2 + L_1 L_2 C_f s^{(\alpha_1+\alpha_2+\beta)}\right) \boldsymbol{I}}. \tag{19}$$

TABLE II
FRACTIONAL ORDER DESCRIPTION

| Symbol | Description | Value |
|---|---|---|
| $\alpha_1$ | Fractional order of $L_1$ | 0.8 |
| $\alpha_2$ | Fractional order of $L_2$ | 0.8 |
| $\beta$ | Fractional order of $C_f$ | 1.1 |

TABLE III
PARAMETER SPECIFICATIONS

| Symbol | Description | Value |
|---|---|---|
| $U_{\mathrm{dc}}$ | DC voltage | 720 V |
| $v_{g_d}^s$ | Grid voltage of d frame | 311 V |
| $i_{g_{ref}}^s$ | Reference grid current of d frame | 20 A |
| $L_g$ | Grid inductance | 0.002 $mH$ |
| $R_g$ | Grid resistance | 0.001 Ω |
| $k_{pll_p}$ | Proportional gain of PLL | 1.72 |
| $k_{pll_i}$ | Integral gain of PLL | 0.5 |
| $k_{PI_p}$ | Proportional gain of PI controller | 27 |
| $k_{PI_i}$ | Integral gain of PI controller | 1523 |
| $f$ | Fundamental frequency | 50 Hz |
| $T_s$ | Sample time | 20 $\mu s$ |
| $L_1$ | Converter side inductance | 0.625 $mH$ |
| $L_2$ | Grid side inductance | 0.15 $mH$ |
| $C_f$ | Filter capacitance | 8 $\mu F$ |
| $R_C$ | Capacitance side resistance | 0.001 Ω |

### E. Accuracy Comparison of Fractional Admittance Model

FO in real circuits can be obtained by the voltage step response combined with least squares, etc., but how to measure the exact filter order is beyond the focus of this article. According to the existing fractional-order system research, the order of the inductor and capacitor is usually between [0,2], so the FO selected in the simulation and experiments in this article is given in Table II.

To verify the higher accuracy of fractional-order admittance, a simulation model of the FLCL-3LT$^2$C with the parameter in Table III was built in MATLAB/Simulink. The converter is treated as a black box, and the small-signal voltage perturbations with different frequency are applied on the grid side [26]. This allows obtaining the magnitude-frequency characteristics sampling points of positive- and negative- sequence impedance in the range of $[10^0, 10^4]$ Hz, represented as orange dots in Figs. 4 and 5. Both integer-order model and FLCL-3LT$^2$C mathematical admittance models $Y_{pp\_IO}$, $Y_{nn\_IO}$ and $Y_{pp\_FO}$, $Y_{nn\_FO}$ were compared in the Bode plot, along with the sampled points of the simulation model, as shown in Fig. 4.

It can be observed that the positive sequence admittance is inductive in the low-frequency and high-frequency bands with the phase approaching 90°. In the mid-frequency range, it becomes capacitive, with the phase approaching −90°. It also exhibits a dip in the frequency response at the fundamental frequency, indicating a significant ability to suppress the current. On the other hand, the negative sequence admittance is capacitive in the mid-low frequency band, with the phase approaching -90°, and inductive in the high-frequency range.

Fig. 5 shows the Bode diagram of the coupling positive-sequence [see Fig. 5(a)] and negative- sequence admittance

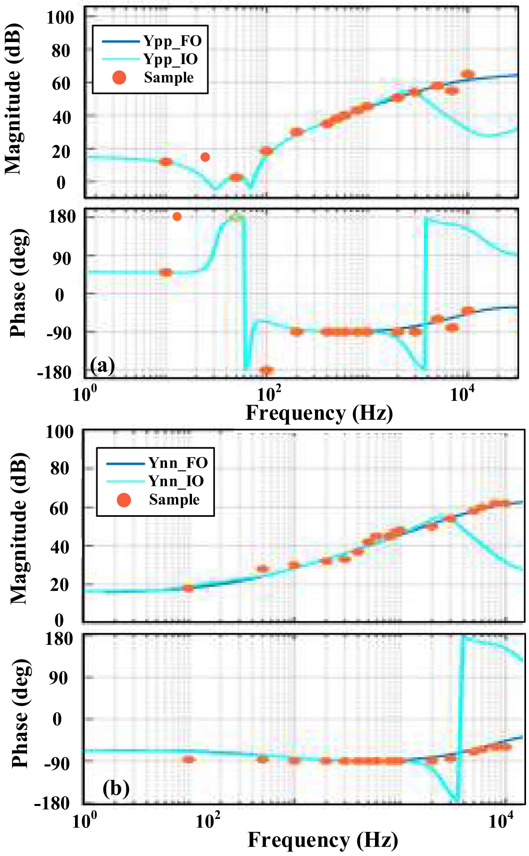

Fig. 4. Bode plot of the positive- and negative-sequence admittance comparison with FO- and IO-mathematical model as well as switching model. (a) Positive sequence admittance. (b) Negative sequence admittance.

model [see Fig. 5(b)] of IO-3LT$^2$C and FLCL-3LT$^2$C, where $Y_{pn\_IO}$ and $Y_{np\_IO}$ represent the integer-order admittance model, and $Y_{pn\_FO}$ and $Y_{np\_FO}$ represent the fractional admittance model. The positive coupling admittance frequency responses of the IO-model and FO-model are not significantly different in the whole frequency range. However, at the turning point, it can still be seen that the response of the fractional-order admittance-frequency characteristics is more closely fitted to the sampling points by simulation. The negative coupling responses of IO and FLCL-3LT$^2$C exhibits inductive at low frequency band and capacitive at mid-frequency band. However, the FO-model would crossover the 180° line at high frequency range.

In summary, although there are some differences at certain frequency points sampling, the cc mathematical model is closer to the magnitude- and phase-response curves formed by the sampled points of the actual model compared to the IO model. This verifies the accuracy of the FO positive and negative sequence admittance model derived in (19), which could be applied in the followed analysis. Since the IO- and FO- admittance models differ greatly in the low and middle frequency bands, with some bands showing completely opposite inductance and capacitance characteristics, the application of IO- model matrices for subsequent stability margin analyses would result in large errors in the calculation of the critical stability point**.**

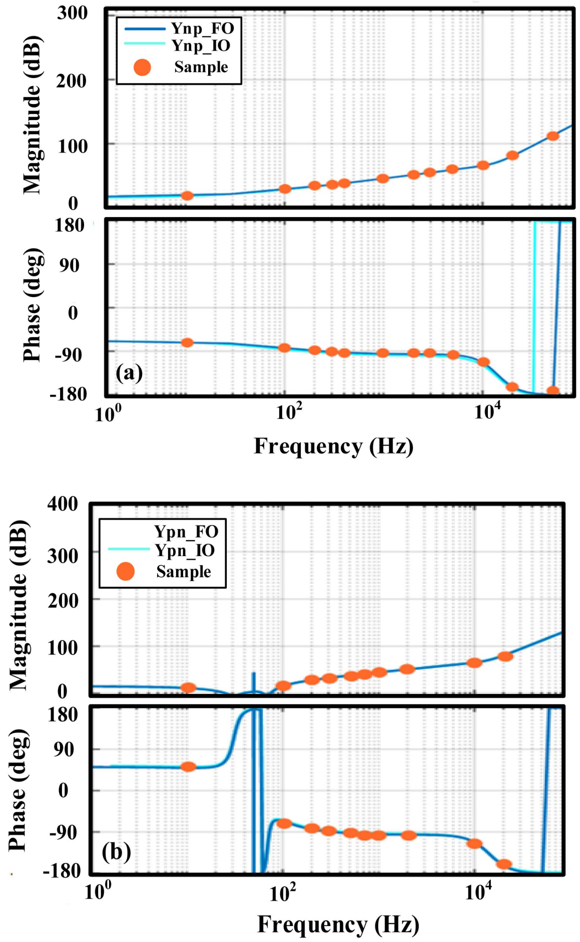

Fig. 5. Bode diagram comparison of the coupling positive- and negative-sequence admittance with FO- and IO-model as well as switching model. (a) Positive coupling sequence admittance. (b) Negative coupling sequence admittance.

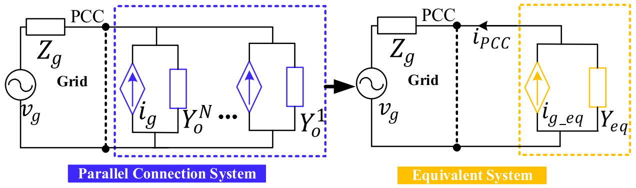

Fig. 6. Equivalent circuit of multiparallel FLCL-3LT$^2$C converters.

## IV. ADMITTANCE MODEL OF PARALLEL GRID-CONNECTED FLCL-3LT$^2$C CONVERTER

### A. Equivalent Model

Since the system model is based on the admittance and current source, when there are $N$ times FLCL-3LT$^2$C connected in parallel, the equivalence output admittance $Y_{\mathrm{eq}}$(see Fig. 5) can be expressed as

$$\boldsymbol{Y}_{\mathrm{eq}} = \sum_{n=1}^{N} \boldsymbol{Y}_o^n = N\boldsymbol{Y}_o. \tag{20}$$

The equivalent circuit is shown in Fig. 6, where $i_{\mathrm{PCC}}$ is the PCC current, $Z_g$ is the grid impedance. Based on Fig. 6, the expression of the PCC current $i_{\mathrm{PCC}}$ is derived as

$$i_{PCC}(s) = \frac{1}{(1+N\boldsymbol{Z_g}(s)\boldsymbol{Y_o}(s))}(Ni_g(s) - Nv_g(s)\boldsymbol{Y_o}(s)). \tag{21}$$

The grid impedance $Z_g$ is composed with grid inductance and grid resistance, whose expression is as

$$\boldsymbol{Z_g} = \frac{1}{3}\begin{bmatrix} Z_{ga}+Z_{gb}+Z_{gc} & Z_{ga}+\alpha^2 Z_{gb}+\alpha Z_{gc} \\ Z_{ga}+\alpha Z_{gb}+\alpha^2 Z_{gc} & Z_{ga}+Z_{gb}+Z_{gc}\end{bmatrix},$$

$$\begin{cases} Z_{ga} = sL_{ga}+R_{ga} \\ Z_{gb} = sL_{gb}+R_{gb} \\ Z_{ga} = sL_{gc}+R_{gc}\end{cases}. \tag{22}$$

### B. Loop Gain Derivation of the System

According to (21), when the grid impedance $Z_g$ is 0, the system model do not contain the poles in the right-half-plane, so the system stability is determined by $\boldsymbol{M}(s) = (1+N\boldsymbol{Z_g}(s)\boldsymbol{Y_o}(s))^{-1}$. If $\boldsymbol{M}(s)$ is equivalent to a negative feedback loop system with a forward path transfer function of 1 and a feedback path transfer function of $N\boldsymbol{Z_g}(s)\boldsymbol{Y_o}(s)$, then $N\boldsymbol{Z_g}(s)\boldsymbol{Y_o}(s)$ is the equivalent loop gain of the system, defined as loop gain $\boldsymbol{L}(s)$. At this point, the system stability can be determined by whether $\boldsymbol{L}(s)$ satisfies the Nyquist stability criterion

$$\boldsymbol{L}(s) = N\boldsymbol{Z_g}(s)\boldsymbol{Y_o}(s) = \begin{bmatrix} L_{pp}(s) & L_{pn}(s) \\ L_{np}(s) & L_{nn}(s)\end{bmatrix}. \tag{23}$$

The loop gain $\boldsymbol{L}(s)$ is a 2 × 2 matrix, therefore the inverse Nyquist array (INA) in multivariable frequency domain analysis could be applied. The principle of INA is to determine system stability by analyzing whether the inverse matrix of the feedback loop matrix satisfies the diagonal dominance. In this article, this inverse matrix happens to be $\boldsymbol{L}(s)$. To calculate whether $\boldsymbol{L}(s)$ has the property of diagonal dominance, this article introduces an eigenvalue estimation method based on the disk theory.

Different with the Nyquist Criterion, this method does not directly calculate the eigenvalues of $\boldsymbol{L}(s)$ to determine the system stability. Instead, it uses the disk theories from matrix theorem to estimate the range of the eigenvalues. If the estimated eigenvalues of $\boldsymbol{L}(s)$ enclose the point (−1,0) on the complex plane, then the system is unstable. This method is based on the traditional Nyquist Criterion but does not require large calculation of the eigenvalues. This significantly reduces the computational complexity, especially for high-order systems where $\boldsymbol{L}(s)$ is complex and challenging to solve. The following sections will explain the two disk theories to estimate the eigenvalues of the $\boldsymbol{L}(s)$.

Therefore, based on the admittance model proposed by the FLCL-3LT$^2$C, this article reduces the computational complexity of stability analysis and critical stability points from the following two aspects.

1) No need to calculate the inverse matrix form of the feedback path.

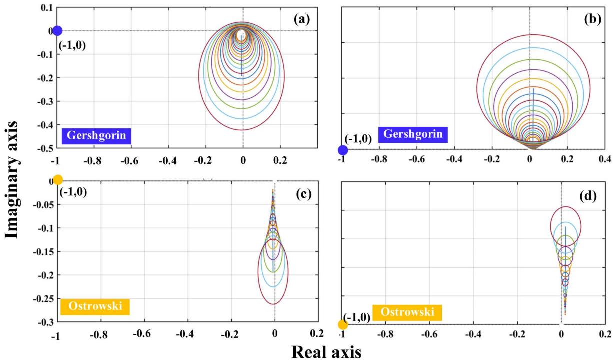

Fig. 7. Disc band of the stable system. (a) and (b) Gershgorin disc band. (c) and (d) Ostrowski disc band.

2) No need to calculate the exact values of the eigenvalues.

## V. STABILITY ANALYSIS

### A. Preliminary of Gershgorin and Ostrowski Theorems

Assume the matrix $\boldsymbol{A}$ is on the complex plane as

$$\boldsymbol{A} = \begin{bmatrix} a_{11} & \cdots & a_{1n} \\ \vdots & \ddots & \vdots \\ a_{n1} & \cdots & a_{nn}\end{bmatrix}. \tag{24}$$

The eigenvalues $\lambda_1, \lambda_2, \ldots, \lambda_n$ would fall within the union of n disks band on complex plane, denoted as $S(\boldsymbol{A})$. There are mainly two disk theories to calculate the union, Gershgorin theorem $S(\boldsymbol{A})_G$ and Ostrowski theorem $S(\boldsymbol{A})_O$, and their expressions are shown as

$$\text{Gershgorin}: \; S(\boldsymbol{A})_G = \bigcup_{x=1}^{n} \{z : |z - a_{xx}| \le R_x, \quad R_x = \sum_{\substack{y=1\\ y\neq x}}^{n} |a_{xy}|\} \tag{25}$$

$$\text{Ostrowski}: \; S(\boldsymbol{A})_O = \bigcup_{x=1}^{n} \{z : |z - a_{xx} \le \sum_{\substack{y=1\\ y\neq x}}^{n} |a_{xy}| \sum_{\substack{y=1\\ y\neq x}}^{n} |a_{yx}||\}. \tag{26}$$

Substituting $\boldsymbol{L}(s)$ into (25) and (26) with the frequency bandwidth selected as $[0, 1e^4]$ Hz and sampling at intervals of 500 Hz, it is possible to plot the circular bands formed by 20 Gershgorin and Ostrowski discs on the complex plane, as shown in Fig. 7. From the figure, it can be observed that the circular bands formed by the Ostrowski theorem are narrower compared to the Gershgorin ranges, occupying a smaller space on the complex plane. Therefore, the critical stability points determined by Ostrowski are less conservative and yield more accurate results.

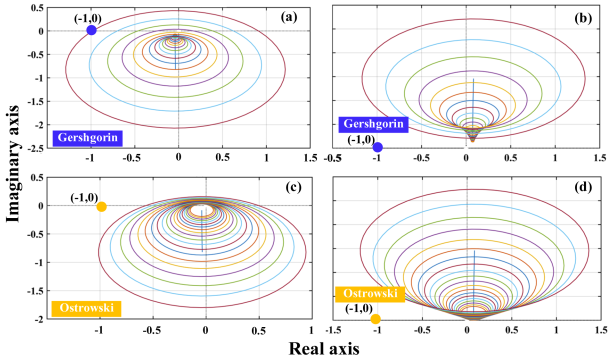

Fig. 8. Disc band of critical stable system determined by Gershgorin theorem. (a) and (b) Gershgorin disc band. (c) and (d) Ostrowski disc band.

### *B. Stability Verification*

The distance between the $S(\boldsymbol{A})_O$ discs band formed by the eigenvalues of $\boldsymbol{L}(s)$ and the point $(-1,0)$ is mainly influenced by three factors: the output admittance $Y_o$, the grid impedance $Z_g$, and the number of parallel-connected converters $N$. Therefore, the effects of unbalanced grid impedance and the addition of positive- and negative sequence harmonics in the grid voltage are separately considered in the simulation. By changing the number of parallel-connected converters $N$, the transformation trend of $S(\boldsymbol{A})_G$ and $S(\boldsymbol{A})_O$ in the complex plane is observed from Fig. 8. It can be observed that as $N$ increases, the radii of the two theoretical disc bands become larger, and the distance to the point (-1, 0) becomes smaller. By this method, the critical stability point can be determined when the disc band just encloses $(-1,0)$ as

$$\begin{cases} D_p = \sqrt{(\mathrm{Im}(L_{\mathrm{pp}}(\omega)))^2 + (\mathrm{Re}(L_{\mathrm{pp}}(\omega))+1)^2} \\ \qquad - |L_{pn}(\omega)|\,|L_{np}(\omega)| \\ D_n = \sqrt{(\mathrm{Im}(L_{nn}(\omega)))^2 + (\mathrm{Re}(L_{nn}(\omega))+1)^2} \\ \qquad - |L_{np}(\omega)|\,|L_{pn}(\omega)| \end{cases}. \quad (27)$$

By (27), we can determine the maximum number of parallel-connected converters of the system. The calculation procedure is shown in Fig. 9.

### *C. Operation Time Comparison*

Fig. 10 compares the time required to calculate the Nyquist criterion, Gershgorin theorem and Ostrowski theorems to determine the system stability when the parallel converter number is 10, and there are positive sequence harmonic components in the grid voltage, respectively. Since disc theorem only estimates the eigenvalues of $\boldsymbol{L}(s)$, the amount of operations required is less than that of the Nyquist criterion (about 5.037 s), which reduces the computational cost, and Ostrowski takes slightly less operation time (about 0.194 s) than Gershgorin theorem. In Fig. 10, the computational time for the two disk theories is the time after going through the full iteration, whereas the traditional stability criterion is the time to plot a single Nyquist curve.

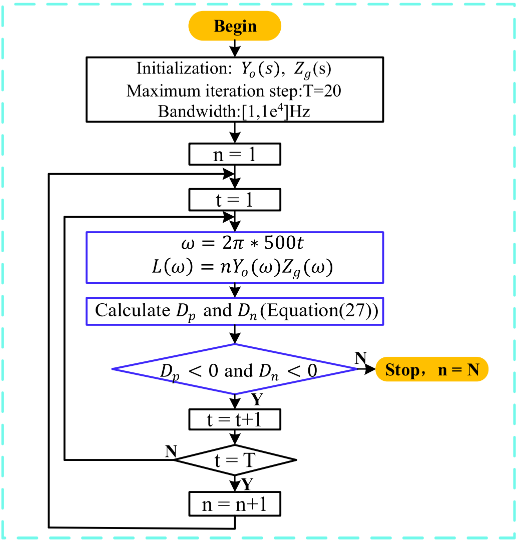

Fig. 9. Implementation steps to determine the critical stability point.

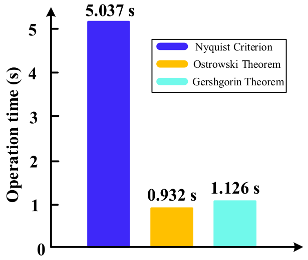

Fig. 10. Operation time comparison.

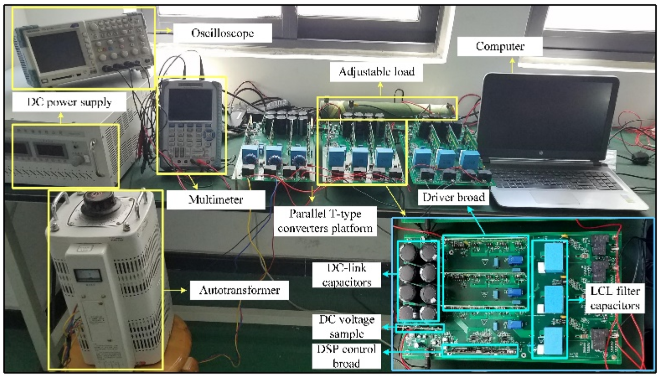

Fig. 11. Hardware setup.

## VI. EXPERIMENTAL RESULTS

### *A. Hardware Setup*

The laboratory platform was set up as shown in Fig. 11. In experiment, the parallel FLCL-3LT$^2$C was operated with a 32-bit floating-point digital signal processor (TMS320F28379, Texas Instrument Company), which is typically used for fast and complex digital calculation and control algorithm implementation. One of the parallel FLCL-3LT$^2$C consists of six

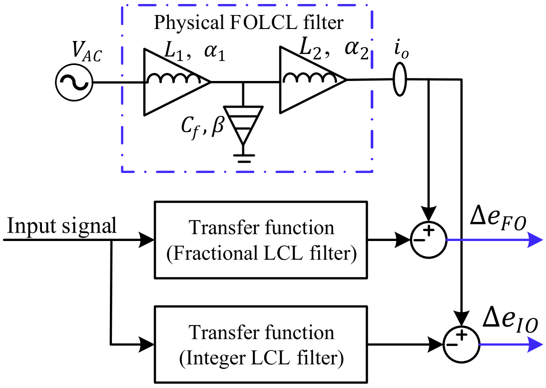

Fig. 12. Comparison of the tracking error with different modeling methods.

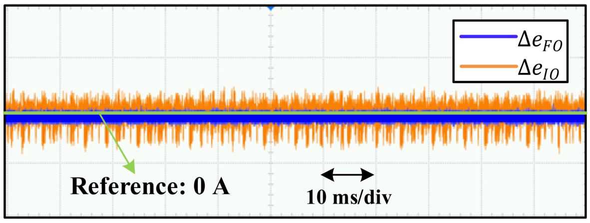

Fig. 13. Tracking error comparison with different modeling methods.

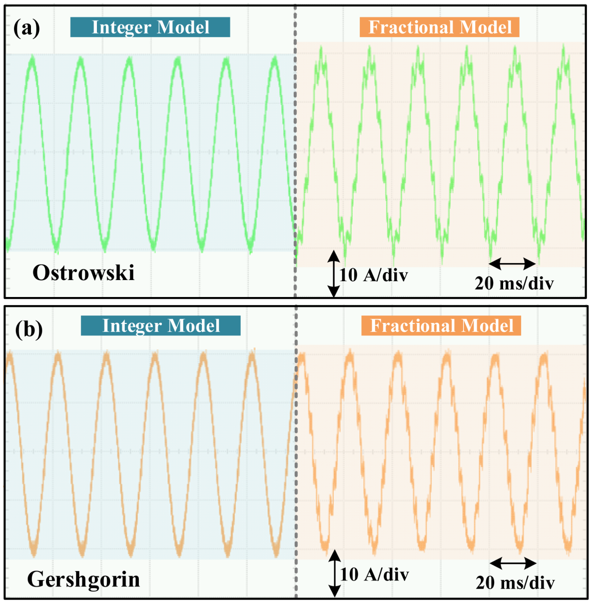

Fig. 14. PCC current at critical stable point calculated by integer model and fractional model. (a) Ostrowski criterion. (b) Gershgorin criterion.

1MBH50D-060 (600 V/50 A) IGBTs with $t_{rr}$ of 0.6 $\mu$s and six 2MBI150U2A-060 (600 V/150 A) IGBTs with $t_{rr}$ of 0.35 $\mu$s for vertical and horizontal bridges from FUZI company. Three Hall current sensors (HCS-LTS-06A) were used to measure grid current. The amplifier OPA4350 was used for grid voltage detection. Two series-connected dc-link capacitors (560 $\mu$F/600 V) were used. A fundamental-frequency three-phase isolation transformer was applied for voltage matching between the output and grid voltages.

To evaluate the accuracy of critical stability point based on different estimation methods (Gershgorin and Ostrowski theorem), two different unbalanced grid scenarios are set to test the quality of the PCC current: unbalanced grid with phase-A grid voltage dropping by 40%; andunbalanced three-phase grid impedance. The results indicate that the critical stability point calculated by Ostrowski theorem has higher accuracy. The related parameters and FOs are given in Tables II and III.

### B. Comparison Between Fractional and Integer Model

*1) Tracking Error Comparison Between Different Modeling Methods:* To verify that the controller parameters designed according to the FO model have better control effects, the open-loop response $i_o$ of an ac voltage $V_{\mathrm{AC}}$(amplitude $=$ 10 V, frequency $=$ 50 Hz) is applied on a physical FLCL circuit, the filter parameters are given in Tables II and III. When $\mathrm{V}_{\mathrm{AC}}$ is applied to the fractional- and integer model the differences between the outputs and $i_o$ are tracking errors, defined as $\Delta e_{FO}$ and $\Delta e_{IO}$ (see Fig. 12). The filter parameters for integral model are given in Table III. The tracking error response of fractional model is closer to 0, the peak-to-peak value of integral tracking error $\Delta e_{IO}$ is about 0.83 A, shown in Fig. 13.

*2) Accuracy Comparison of Stability Margin Calculation With Different Modeling Method:* Apply mathematical models based on fractional- and integer-order filter, then calculate the critical stability points under balanced grid conditions. The results of the two sets of criteria are shown in Fig. 14. When the parallel capacity exceeds the critical stability point determined by the integer-order model, the PCC current can maintain stable output, with the total harmonic distortion (THD) of less than 5%. Conversely, the critical stability point calculated using fractional-order model is more accurate. Beyond this critical stability point, different degrees of resonance occur in the PCC current, with THD of 12.98% in Fig. 14(a) and 8.52% in Fig. 14(b).

### C. Critical Stability Point Determination of FLCL-3LT$^2$C Under Unbalanced Grid

The amplitude of the grid voltage in phase-B drops by 40% to simulate the unbalanced grid condition. The waveform of the unbalanced three-phase grid voltage is shown in Fig. 15.

From the derivation results in Sections III and IV, it could be seen that the unbalanced grid will cause the phase angle error of the phase-locked loop, thus changing the equivalent output admittance $Y_o(s)$ of the parallel FLCL-3LT$^2$C system.

*1) Critical Stability Point Determination With Gershgorin Theorem:* According to the derivation and implementation flowchart in Section V, it can be concluded that the maximum parallel FLCL-3LT$^2$C calculated by Gershgorin stability criterion is 126. Fig. 16(a) shows the waveform of the PCC current at $N = 127$ under the critical instability condition. The output current obviously contains more harmonics, and the THD is about 4.86% shown in the FFT analysis of Fig. 16(b). The critical stable

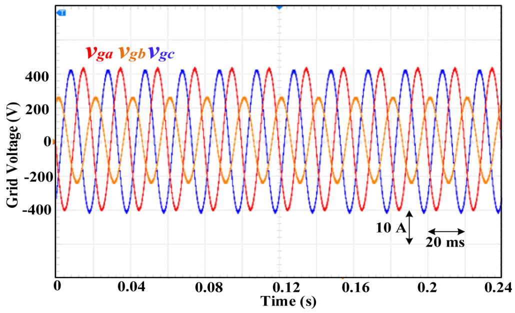

Fig. 15. Waveform of the grid voltage.

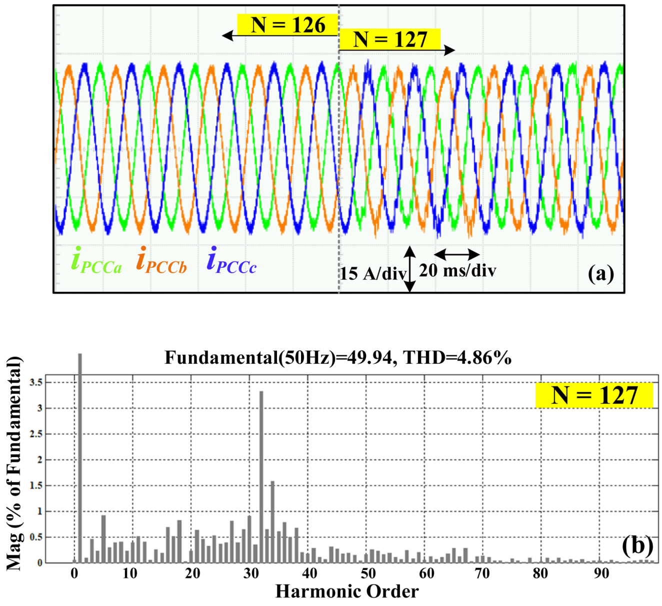

Fig. 16. Critical stable point calculated by Gershgorin theorem. (a) Dynamic response of PCC current. (b) FFT analysis when $N = 127$.

point judged by Gershgorin criterion in the case of single-phase grid voltage drop shows that, although the harmonic content of PCC current is higher than the stable condition (0.74%), the phase balance of three-phase current can still be maintained, and the PCC current would not diverge.

*2) Critical Stability Point Determination With Ostrowski Theorem:* According to the derivation results in Section IV, the maximum parallel units $N$ calculated by Ostrowski stability criterion is 145. Fig. 17 shows the three-phase PCC current at $N = 146$ under critical instability conditions. First, the amplitude of the reference current is 20 A. However, Fig. 17(a) shows that the peak output current changes from 8 to 30 A and has an increasing trend. Second, the three-phase output currents are unbalanced, and their periods could not maintain 50 Hz, the frequency is smaller than the fundamental frequency, and the PCC current is periodically oscillating. Meanwhile the THD of $N = 146$ increases to 70.57% in FFT analysis of Fig. 17(b). In this case, the output current is completely unstable, which may endanger the system stability and even case serious damage the power electronic devices.

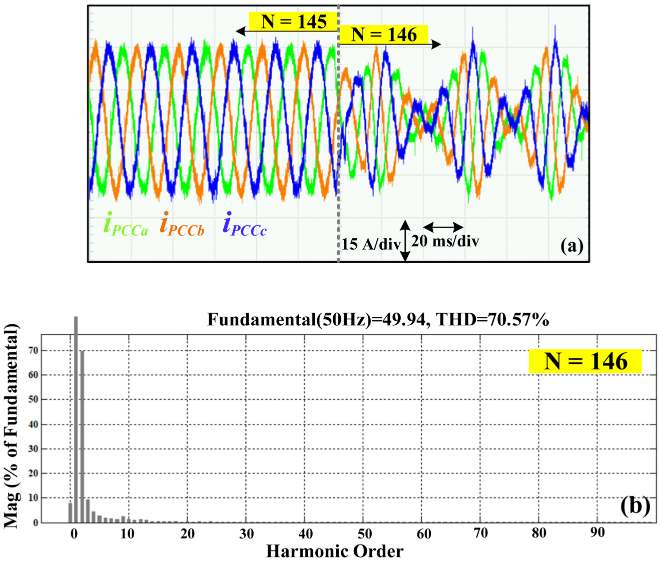

Fig. 17. Critical stable point calculated by Ostrowski theorem. (a) Dynamic response of PCC current. (b) FFT analysis when $N = 146$.

### *D. Critical Stability Point of FLCL-3LT$^2$C Unbalanced Grid Impedance*

This part of experiment verifies the accuracy of stability criteria in determining the critical stability point of the system when the three-phase grid impedance is unbalanced. The grid inductance $L_g$of a single FLCL-3LT$^2$C in $abc$-phases is given as follows:

$$\begin{cases} L_{ga} = 2\ \mu\text{H} \\ L_{gb} = 5\ \mu\text{H} \\ L_{gc} = 2\ \mu\text{H} \end{cases}. \tag{28}$$

Based on (28), the equivalent grid impedance $Z_{g\_\text{eq}}$ of the parallel FLCL-3LT$^2$C system is

$$Z_{g\_\text{eq}} = N Z_g. \tag{29}$$

*1) Critical Stability Point With Gershgorin Theorem:* From the simulation results When the grid impedance is unbalanced, the critical stability point calculated by Gershgorin band is achieved with $N = 103$.

In experiment (see Fig. 18), as the parallel converter number increases to 104, the peak current of phase $b$ is 12.3 A, which is significantly lower than the peak currents of phases-$a$ and -$c$ at 21.7 A. Although there is severe distortion and peak amplitude imbalance in the three-phase current (with single-phase THD increasing to 27.87%), the frequency of the PCC current remains at the fundamental frequency of 50 Hz. The current peaks do not diverge but fluctuate around the peak value of the reference current.

*2) Critical Stability Point Based on Ostrowski Theorem:* According to the simulation results in Section V, the critical stability point determined by the Ostrowski band occurs when $N = 137$. The grid current waveform when the parallel number of converters is 138 is shown in Fig. 19.

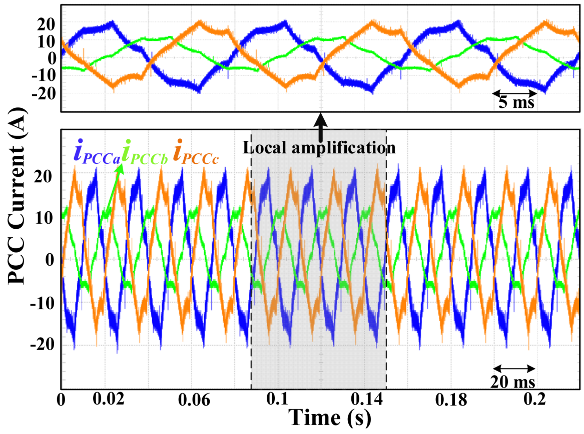

Fig. 18. PCC current $i_{PCC}$ with unbalanced grid impedance when $N = 104$.

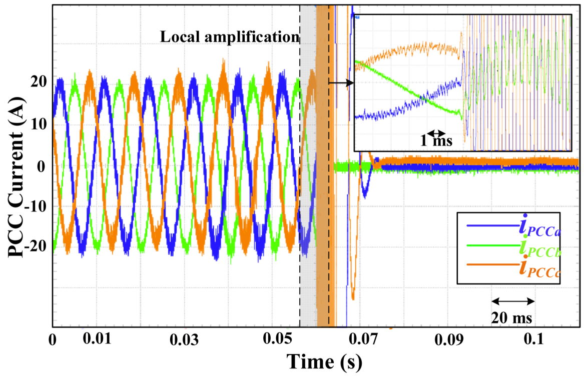

Fig. 19. PCC current with unbalanced grid impedance from $N = 10$ to $N = 138$.

At this point, the three-phase PCC currents exhibit divergence. The current peaks would greatly oscillate, significantly exceeding the reference current 20 A. However, to prevent the hazards caused by excessive grid current, the converter would be disconnected to the grid when the root-mean-square value of the PCC current is greater than 40 A. From the amplified section, it can be observed that the current frequency at this point is approximately 2.5 kHz. Furthermore, the current frequency increases with the increasing oscillation peak amplitude, indicating severe system instability.

### *E. Stability Analysis of Parallel FLCL-3LT$^2$C With Different Filter Parameters*

To verify that the improved stability criterion proposed in this article is also applicable to parallel systems with different filter parameters, two parallel converters were used (see Fig. 20) and defined as Groups A and B, with their filter parameters and converter capacities given in Tables IV and V, respectively. The FO of an LCL filter used here is given in Table II

*1) Dynamic Response of the Converter Output Current:* Fig. 21 illustrates the operating conditions with a fixed number of 2 converters in Group A and varying units of group B connected to the grid. Based on the simulation results shown in Fig. 9, the Gershgorin theory calculates the maximum parallel operation scale as 72 units, while the Ostrowski theory suggests 85 units. In Fig. 18, the left-side of the dashed line represents the scenario where the equivalent grid impedance reaches the critical stability point determined by Gershgorin, while the right side represents the Ostrowski stability criterion. Concerning the grid-side impedance of both A and B group converters, when the output current reaches the maximum stable margin as per the Ostrowski theory, there is a significant increase in THD leading to severe waveform distortion.

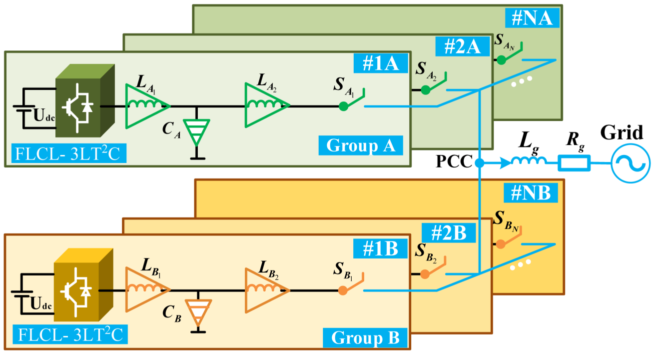

Fig. 20. Switching states of the FLCL-3LT$^2$C with different filters.

TABLE IV
PARAMETERS OF GROUP A

| Symbol | Description | Value |
|---|---|---|
| $P_A$ | Power rate | 10 kW |
| $L_{A_1}$ | Converter side inductance | 0.625 mH |
| $L_{A_2}$ | Grid-side inductance | 0.15 mH |
| $C_A$ | Capacitance | 10 $\mu$F |
| $k_{A_{PI\_p}}$ | Proportional gain of PI controller | 0.45 |
| $k_{A_{PI\_i}}$ | Integral gain of PI controller | 1350 |

TABLE V
PARAMETERS OF GROUP B

| Symbol | Description | Value |
|---|---|---|
| $P_B$ | Power rate | 8 kW |
| $L_{B_1}$ | Converter side inductance | 0.45 mH |
| $L_{B_2}$ | Grid inductance | 0.2 mH |
| $C_B$ | Capacitance | 10 $\mu$F |
| $k_{B_{PI\_p}}$ | Proportional gain of PI controller | 0.5 |
| $k_{B_{PI\_i}}$ | Integral gain of PI controller | 950 |

*2) Dynamic Response of PCC Current:* Fig. 22 depicts the waveforms of the three-phase PCC current under critical stable margin conditions calculated using two different disk theories, with the dashed line indicating the boundary. As the equivalent grid impedance increases to the critical stability point according to the Gershgorin theory, the voltage and current at the PCC remain stable and maintain three-phase balance. However, if the impedance rises to the critical stability point based on the Ostrowski theory, significant waveform distortion occurs in the voltage and current outputs. In Fig. 23, it is demonstrated that when the equivalent grid impedance surpasses the critical stability point calculated by the Ostrowski theory, the THD of the PCC current reaches approximately 14.73%, indicating a high level of harmonics that do not meet grid connection standards.

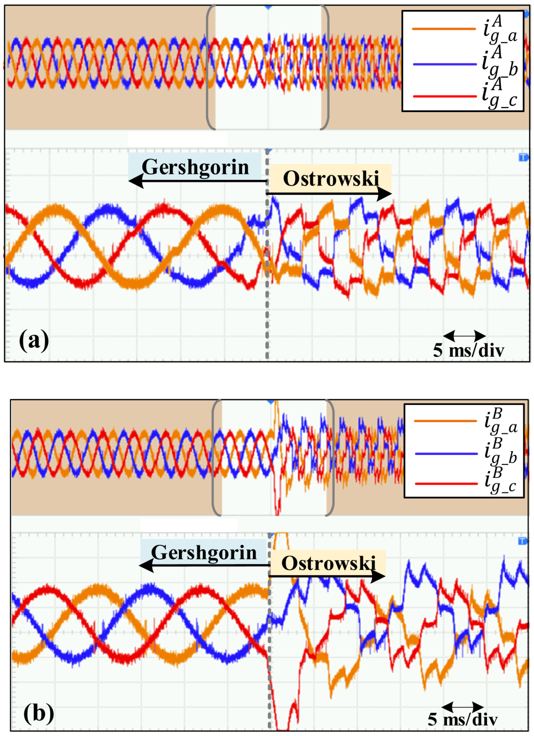

Fig. 21. Grid current of groups A and B. (a) Group A. (b) Group B.

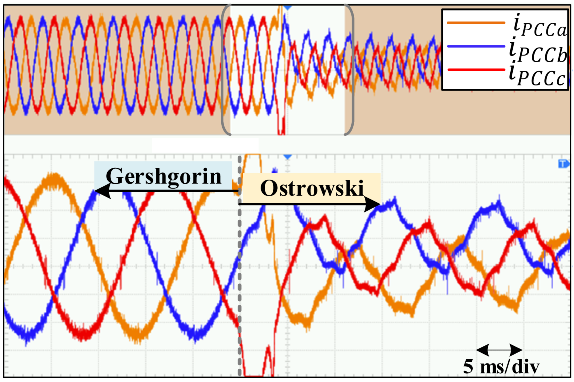

Fig. 22. PCC current under different stability criterion.

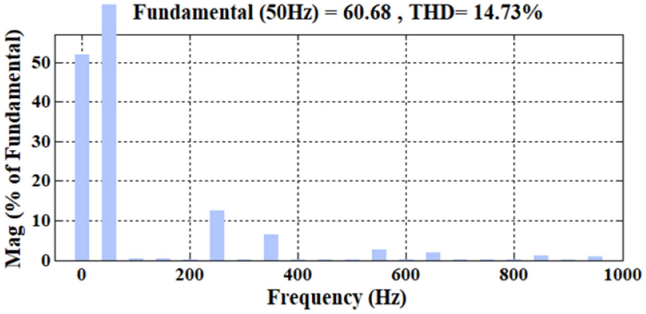

Fig. 23. FFT analysis of PCC current.

TABLE VI
CONSERVATIVENESS COMPARISON OF THE CRITICAL STABILITY POINT WITH GERSHGORIN AND OSTROWSKI METHODS

| Maximum $N$ with different stability theorem | Imbalanced grid voltage | Imbalanced Grid impedance | PCC current |
|---|---|---|---|
| Gershgorin | 126 | 103 | Distorted |
| Ostrowski | 145 | 137 | Unstable |

This situation could potentially lead to damage to the power electronic devices connected to the grid.

### *F. Summary*

Equation (23) indicates that $\boldsymbol{L}(s)$ is mainly affected by the number of shunt units $N$, the system admittance $\boldsymbol{Y_o}$ and the grid impedance $\boldsymbol{Z_g}$. Then the experiments are divided into two unbalanced grid conditions (Section VI-C for grid voltage drop to change $\boldsymbol{Y_o}$, and Section VI-D for grid impedance unbalance to influence $\boldsymbol{Z_g}$), while the Gershgorin and Ostrowski theorems are used to calculate the critical stability point, i.e., the maximum parallel FLCL-3LT$^2$C converter number that can be connected to the grid. From Table VI, the critical stability point calculated by Gershgorin theorem only makes the grid side current distortion more severe, while the critical stability point calculated by Ostrowski theorem makes the system completely destabilized and oscillating. Therefore, the critical stability estimation method based on Ostrowski theorem is more accurate and less conservative.

## VII. CONCLUSION

This article investigates the critical stability point estimation of the parallel FLCL-3LT$^2$C system under unbalanced grid. First, the factional order mathematical model of parallel LCL-3LT$^2$C is established; second, the Ostrowski theorem is applied to estimate the stability margin based on the loop gain of the coupling system of FLCL-3LT$^2$C and unbalanced grid. The proposed fractional admittance improves the model accuracy compared with the traditional integer model and the stability analysis method in this article effectively reduces the computational burden and the conservativeness compared with traditional stability analysis methods.

## REFERENCES

[1] Z. Xin, P. Mattavelli, W. Yao, Y. Yang, F. Blaabjerg, and P. C. Loh, "Mitigation of grid-current distortion for LCL-filtered voltage-source inverter with inverter-current feedback control," *IEEE Trans. Power Electron.*, vol. 33, no. 7, pp. 6248–6261, Jul. 2018.

[2] N. A. Ashtiani, A. Sheykhi, and S. A. Khajehoddin, "Modified droop strategy for wide load range efficiency improvement of parallel inverter systems," *IEEE Trans. Power Electron.*, vol. 37, no. 7, pp. 8433–8446, Jul. 2022.

[3] A. A. Nazib, D. G. Holmes, and B. P. McGrath, "Self-synchronizing stationary frame inverter-current-feedback control for LCL grid-connected inverters," *IEEE J. Emerg. Sel. Topics Power Electron.*, vol. 10, no. 2, pp. 1434–1446, Apr. 2022.

[4] C.-Y. Tang and J.-H. Jheng, "An active power ripple mitigation strategy for three-phase grid-tied inverters under unbalanced grid voltages," *IEEE Trans. Power Electron.*, vol. 38, no. 1, pp. 27–33, Jan. 2023.

[5] S. Luo, W. Wu, E. Koutroulis, H. S.-H. Chung, and F. Blaabjerg, "A new unbalanced voltage compensation method based on HOPF oscillator for three-phase DC/AC inverters with unbalanced loads," *IEEE Trans. Smart Grid*, vol. 13, no. 6, pp. 4245–4255, Nov. 2022.

[6] L. Zhang, A. Kartci, A. Elwakil, H. Bagci, and K. N. Salama, "Fractional-order inductor: Design, simulation, and implementation," *IEEE Access*, vol. 9, pp. 73695–73702, May 2021.

[7] Y. Jiang and B. Zhang, "Comparative study of Riemann–Liouville and Caputo derivative definitions in time-domain analysis of fractional-order capacitor," *IEEE Trans. Circuits Syst. II: Exp. Briefs*, vol. 67, no. 10, pp. 2184–2188, Oct. 2020.

[8] B. Long, P. J. Lu, K. T. Chong, J. Rodriguez, and J. Guerrero, "Robust fuzzy-fractional-order nonsingular terminal sliding-mode control of LCL-type grid-connected converters," *IEEE Trans. Ind. Electron.*, vol. 69, no. 6, pp. 5854–5866, Jun. 2022.

[9] A. Zafari, M. Mehrasa, S. Bacha, K. Al-Haddad, and N. Hosseinzadeh, "A robust fractional-order control technique for stable performance of multilevel converter-based grid-tied DG units," *IEEE Trans. Ind. Electron.*, vol. 69, no. 10, pp. 10192–10201, Oct. 2022.

[10] B. Babes, S. Mekhilef, A. Boutaghane, and L. Rahmani, "Fuzzy approximation-based fractional-order nonsingular terminal sliding mode controller for DC–DC buck converters," *IEEE Trans. Power Electron.*, vol. 37, no. 3, pp. 2749–2760, Mar. 2022.

[11] X. Lin, J. Liu, F. Liu, Z. Liu, Y. Gao, and G. Sun, "Fractional-order sliding mode approach of buck converters with mismatched disturbances," *IEEE Trans. Circuits Syst. I: Regular Papers*, vol. 68, no. 9, pp. 3890–3900, Sep. 2021.

[12] M. A. Azghandi, S. M. Barakati, and A. Yazdani, "Impedance-based stability analysis and design of a fractional-order active damper for grid-connected current-source inverters," *IEEE Trans. Sustain. Energy*, vol. 12, no. 1, pp. 599–611, Jan. 2021.

[13] Z. Xie, X. Gao, S. Yang, and X. Zhang, "Improved fractional-order damping method for voltage-controlled DFIG system under weak grid," *J. Modern Power Syst. Clean Energy*, vol. 10, no. 6, pp. 1531–1541, 2022.

[14] B. Zhang, X. Du, J. Zhao, J. Zhou, and X. Zou, "Impedance modeling and stability analysis of three-phase three-level NPC inverter connected to grid," *CSEE J. Power Energy Syst.*, vol. 6, no. 2, pp. 270–278, Jun. 2020.

[15] X. Peng and H. Yang, "Stability analysis of multi-paralleled grid-connected inverters including the distribution parameter characteristics of transmission lines," *CSEE J. Power Energy Syst.*, vol. 7, no. 1, pp. 93–104, Jan. 2021.

[16] W. Wu, X. Lan, H. Li, and B. Ma, "The controller design method of grid-connected inverter based on reduced order Jacobian matrix," in *Proc. Chin. Automat. Congr.*, 2020, pp. 6533–6538, doi: 10.1109/CAC51589.2020.9327665.

[17] H. Makhamreh, M. Sleiman, O. Kukrer, and K. Al-Haddad, "Lyapunov-based model predictive control of a PUC7 grid-connected multilevel inverter," *IEEE Trans. Ind. Electron.*, vol. 66, no. 9, pp. 7012–7021, Sep. 2019.

[18] Y. Han et al., "Floquet-theory-based small-signal stability analysis of single-phase asymmetric multilevel inverters with SRF voltage control," *IEEE Trans. Power Electron.*, vol. 35, no. 3, pp. 3221–3241, Mar. 2020.

[19] B. Shu, M. Gao, D. Zhang, K. Meng, R. N. Ashraf, and Y. Wang, "Control strategy of three-phase inverter under weak grid condition," in *Proc. Int. Conf. Smart Grids Energy Syst.*, 2020, pp. 740–745.

[20] A. Riccobono, M. Mirz, and A. Monti, "Noninvasive online parametric identification of three-phase AC power impedances to assess the stability of grid-tied power electronic inverters in LV networks," *IEEE J. Emerg. Sel. Topics Power Electron.*, vol. 6, no. 2, pp. 629–647, Jun. 2018.

[21] A. Urtasun, J. Samanes, E. L. Barrios, and P. Sanchis, "Control design and stability analysis of power converters: The discrete generalized bode criterion," *IEEE Access*, vol. 9, pp. 37840–37854, Mar. 2021.

[22] Z. Xie, Y. Chen, W. Wu, W. Gong, and J. M. Guerrero, "Stability enhancing voltage feed-forward inverter control method to reduce the effects of phase-locked loop and grid impedance," *IEEE J. Emerg. Sel. Topics Power Electron.*, vol. 9, no. 3, pp. 3000–3009, Jun. 2021.

[23] Y. Ren, R. Duan, L. Chen, W. Huang, C. Wu, and Y. Min, "Stability assessment of grid-connected converter system based on impedance model and Gershgorin theorem," *IEEE Trans. Energy Convers.*, vol. 35, no. 3, pp. 1559–1566, Sep. 2020.

[24] H. Xu, H. Wu, Z. Li, Q. Yan, and F. Blaabjerg, "Gershgorin-circle based low-complexity generalized Nyquist stability criterion for DFIG driven wind turbines," *IEEE J. Emerg. Sel. Topics Circuits Syst.*, vol. 12, no. 1, pp. 29–40, Mar. 2022.

[25] M. Cespedes and S. Jian, "Impedance modeling and analysis of grid-connected voltage-source converters," *IEEE Trans. Power Electron.*, vol. 29, no. 3, pp. 1254–1261, Mar. 2014.

[26] X. Wang, X. Wei, Q. Chen, and H. Dai, "A novel system for measuring alternating current impedance spectra of series-connected lithium-ion batteries with a high-power dual active bridge converter and distributed sampling units," *IEEE Trans. Ind. Electron.*, vol. 68, no. 8, pp. 7380–7390, Aug. 2021.

**Bo Long** (Senior Member) received the B.S. degree in electrical engineering from the Xi'an Petroleum University, Xian, China, in 2001, and the Ph.D. degree in electrical engineering from Xian Jiaotong University, Shanxi, China, in 2008.

He was with the Department of Power Electronics, School of Mechatronics Engineering, University of Electronic Science and Technology of China, in 2008, and has been promoted to an Associate Professor, since 2014. He is currently the supervisor for 11 master students, 2 of which have been nominated as provincial outstanding graduate student of UESTC. His research interests include grid-connected converters for renewable energy systems and DGs, model predictive control, power quality, multilevel converters, ac motor control, and resonance suppression technique for smart grid applications.

**Wandi Yang** received the B.S. degree in electrical and electronic engineering in 2021 from the University of Electronic Science and Technology of China, Chengdu, China, where she is currently working toward the M.S. degree in electric engineering.

Her current research includes the parameter identification of *LCL* filter and stability analysis of parallel connected fractional inverters.

**JieFeng Hu** (Senior Member) received the Ph.D. degree in electrical engineering from the University of Technology Sydney, Ultimo, NSW, Australia, in 2013.

He participated in the research of microgrids at Commonwealth Scientific and Industrial Research Organization, Newcastle, Australia. He was an Assistant Professor with The Hong Kong Polytechnic University, Hong Kong. He is currently an Associate Professor and Stream Leader with the Centre for New Energy Transition Research, Federation University Australia. He is also the Program Coordinator of Electrical Engineering and Renewable Energy. His research interests include power electronics, renewable energy, and smart microgrids.

Dr. Hu is an Editor for IEEE TRANSACTIONS ON ENERGY CONVERSION, an Associate Editor for IEEE ACCESS, and an Associate Editor for *IET Renewable Power Generation*. He was the Lead Guest Editor for IEEE TRANSACTIONS ON INDUSTRIAL ELECTRONICS for a Special Issue "Applications of Predictive Control in Microgrids."

**Jose Rodriguez** (Fellow, IEEE) received the Engineer degree in electrical engineering from the Universidad Tecnica Federico Santa Maria, in Valparaiso, Chile, in 1977 and the Dr.-Ing. degree in electrical engineering from the University of Erlangen, Erlangen, Germany, in 1985.

Since 1977, he has been with the Department of Electronics Engineering, Universidad Tecnica Federico Santa Maria, where he was a Full Professor and the President. Since 2015, he has been the President of Universidad Andres Bello, Santiago, Chile. He has coauthored two books, several book chapters, and more than 400 journal and conference papers. His research interests include multilevel inverters, new converter topologies, control of power converters, and adjustable-speed drives.

**Kil To Chong** (Member) received the Ph.D. degree in mechanical engineering from Texas A&M University, College Station, TX, USA, in 1995.

He is currently a Professor and the Department Head with the School of Electronics and Information Engineering and a Member and the Head of the Advanced Electronics and Information Research Center, Chonbuk National University, Jeonju, South Korea. His research interests include motor fault detection and control, network system control, sensor network systems, time-delay systems, and neural networks.